Journal of Polymers and the Environment (2023) 31:3677–3687
https://doi.org/10.1007/s10924-023-02855-5

ORIGINAL PAPER

Synthesis of PolyHIPEs from Photocurable Water-in-Oil High Internal Phase Emulsions by Using a Sustainable Monomer: β-Myrcene

Meltem Sözbir[1] · Burcu Kekevi[2] · E. Hilal Mert[3]

Accepted: 25 March 2023 / Published online: 7 April 2023

Abstract

Recently, there has been an increasing interest in the synthesis of bio-derived and sustainable polymers due to limited petroleum resources and the dependence of polymer chemistry on fossil fuels. Terpenes which are found in nature in wide variety of structures, are a large family derived from plants. Isoprene like structure of terpenes make these natural compounds susceptible to polymerization. In this work, β-myrcene, which is an acyclic monoterpene was used in the synthesis of photocurable porous polymer monoliths via high internal phase emulsion (HIPE) templating. Photocuring of β-myrcene in HIPE templates has been achieved by the free radical copolymerization crosslinking reaction with 1,4-butanediol dimethacrylate (1,4-BDDMA). To determine the effect of monomer ratio on the crosslink density and pore morphology of the resulting polyHIPEs, the volume ratio of β-myrcene in the external phase has been varied from 10 to 90. Crosslink density of the polyHIPEs has been calculated by swelling experiments using Flory-Rehner Theory. In the end, polyHIPEs exhibiting pore morphology constituted of cavities and interconnected pores has been obtained in all cases. However, it has been determined that 60% is the optimum β-myrcene ratio to obtain a highly crosslinked polyHIPE accompanied with an open-cellular pore morphology.

Keywords Emulsion templating · PolyHIPE · β-myrcene · Photopolymerization · Crosslink density

Introduction

Poly(High Internal Phase Emulsion)s (polyHIPEs) are crosslinked porous polymers prepared via emulsion templating approach. Emulsions are thermodynamically unstable heterogeneous systems composed of immiscible two phases, which are in most of the cases oil and water. HIPEs on the other hand, are emulsions having an internal phase volume fraction (Ø) greater than 0.74. This volume fraction corresponds to the maximum packing ratio of monodisperse and non-deformable spheres. When the external phase of a HIPE consists of monomer(s), polymerization of this phase followed by the removal of internal phase and drying yields polyHIPEs [1–4].

PolyHIPEs may exhibit open-cell or closed-cell pore morphology, depending on the presence of interconnectivity between cavities [5]. Application field of a polyHIPE is determined according to the pore morphology, hydrophobic/hydrophilic nature of the material and chemical functionality [2, 4]. Morphological and mechanical features of a polyHIPE can be tuned by controlling the experimental parameters during emulsion preparation. Monomer composition, dispersed phase ratio, surfactant amount or the amount of nanoparticle loading have a great influence on the cavity diameter, interconnected pore diameter, pore size distribution, pore volume, skeletal density, foam density and mechanical strength [6]. PolyHIPEs are attracting increasing attention in many fields, especially in adsorption [7, 8], chromatography [9, 10], energy storage [11, 12] and tissue engineering [13–15]. PolyHIPEs are usually prepared in monolithic shape [16–18]. However, to provide applicability in different fields they can be also prepared in a wide

✉ Burcu Kekevi
bkekevi@yalova.edu.tr

[1] Department of Polymer Materials Engineering, Institute of Graduate Studies, Yalova University, Yalova 77200, Türkiye

[2] Department of Material and Material Processing Technologies, Yalova University, Yalova Community College, Yalova 77200, Türkiye

[3] Faculty of Engineering, Department of Polymer Materials Engineering, Yalova University, Yalova 77200, Türkiye

variety of forms including beads, rods, fibers, and complex shapes [2].

Hydrophobic polyHIPEs are usually synthesized from water-in-oil (w/o) HIPEs, whereas hydrophilic polyHIPEs are generally obtained from oil-in-water (o/w) HIPEs [2]. By far, thermally initiated free radical polymerization (FRP) is the most widely used polymerization mechanism for polyHIPE synthesis. For this purpose, mostly styrene, divinylbenzene and (meth)acrylate monomers are preferably polymerized by FRP mechanism, in the external phase of HIPEs [19, 20]. However, thermal initiated FRP mechanism has limitations depending on emulsion stability, thermal susceptibility of highly reactive monomers and requirement of long curing periods. Photoinitiated FRP, on the other hand, provides the advantage of rapid polymerization at room temperature without compromising emulsion stability. In this respect, photocurable HIPEs were successfully used for the preparation of scaffolds by 3D-printing and lithography. Until now, polyHIPE scaffolds have been synthesized using the advantages of "click" chemistry on photocurable thiol–ene and thiol–yne based HIPEs and polycaprolactone, polyurethane or acrylate based polyHIPEs [21–24].

Renewable resourced sustainable monomers and resins are attracting interest of researchers from academy and polymer industry due to depletion of fossil sources, and as well as increasing interest in green and environmental manufacturing processes. In this context, there is a growing interest on formulating photocurable resins based on bio-derived and sustainable monomers for advanced manufacturing processes. Photocurable resins have wide range of applications in 3D-printing and lithography, where it is possible to manufacture materials with desired geometry and shape more easily and rapidly [25]. In accordance with this, preparing polyHIPEs from renewable resource monomers is recently became an issue of interest for the researchers. While there are limited number of bio-derived monomer and resin available for industrial manufacturing, terpenes and terpenoids are some of the most promising candidates for the preparation of sustainable bio-derived resins and photocured advanced polymers [26].

Terpenes and terpenoids have wide application in the food, cosmetics, fragrance, and perfume industry, due to their abundance in essential oils, tree saps, and citrus fruits [27]. These bio-derived molecules have a general formula similar with isoprene, and inherent double bonds which make them available for polymerization [28]. In this respect, *β*-myrcene is drawing attention in the development of sustainable biobased elastomers through emulsion copolymerization [29–31]. However, attempts to (co) polymerize *β*-Myrcene through FRP, controlled RP, ionic polymerization or coordination polymerization have shown that these mechanisms are limited in controlling polymer microstructure, branching, molecular weight, and polydispersity, as a result of steric hindrance and monomer reactivity [32]. Development of photocurable *β*-myrcene formulations for 3D-printing applications have been studied with using different thiols [33–35]. In these studies, low polymerization reactivity and low viscosity of the obtained formulations were reported as the main problems encountered [36–40].

In our previous studies, we have been investigated FR copolymerization crosslinking (FRCXL) of *β*-myrcene within HIPEs using several comonomers including styrene, glycidyl methacrylate (GMA), divinylbenzene (DVB), 2-ethyl hexyl acrylate (2-EHA), ethylene glycol dimethacrylate (EGDMA), 4-vinylbenzyl chloride (4-VBC) and 1,3-butanedioldiacrylate (1,3-BDDA). We have been demonstrated with this work that the limitations due to monomer reactivity prevent cross-linking, while highly cross-linked polyHIPEs based on polymyrcene (PMy) copolymers can only be obtained in the presence of comonomers providing free volume [41].

Herein, we have been focused on the preparation of photocurable HIPEs that are containing *β*-myrcene in the external phase. 1,4-butanediol dimethacrylate (1,4-BDDMA) has been used as the crosslinker comonomer. The influence of monomer composition in the external phase on polyHIPE properties has been investigated by varying the ratio of *β*-myrcene to 1,4-BDDMA between 10/90 and 90/10. In the end, crosslink density of polyHIPEs has been calculated with the help of swelling tests and Flory-Rehner Theory. PolyHIPE pore morphology and thermal stability has been also investigated in detail. Moreover, the effect of the initiation step of polymerization mechanism on the final polyHIPE properties has been also investigated with the help of counterpart samples synthesized via thermally initiated FRP.

Experimental

Materials

β-Myrcene (Supelco), 1,4-butanediol dimethacrylate (95%, contains 200–300 ppm MEHQ as inhibitor, Sigma-Aldrich), Span® 80 (viscosity 1000–2000 mPas (20 °C), Supelco), Pluronic® L121 (poly(ethylene glycol)-block-poly(propylene glycol)-block-poly(ethylene glycol), average Mn ~ 4,400, Sigma-Aldrich), pentaerythritol tetrakis(3,5-di-tert-butyl-4-hydroxyhydrocinnamate) (98%, Sigma-Aldrich), potassium persulfate (ACS reagent, ≥ 99.0%, Sigma-Aldrich), 2-hydroxy-4′-(2-hydroxyethoxy)-2-methylpropiophenone (commercially known as Irgacure 2959, 98%, Sigma-Aldrich), calcium chloride hexahydrate

(98%, Sigma-Aldrich) were used as received. Ethanol (99.5%) which was technical grade, purchased from Tekkim Kimya.

PolyHIPE Synthesis

Thermally Cured PolyHIPEs

PolyHIPEs were synthesized by curing HIPEs having dispersed phase ratio of 80 vol%. Continuous phase of HIPEs were composed of β-myrcene, 1,4-BDDMA and surfactant mixture. To prepare HIPEs β-myrcene, 1,4-BDDMA, Span® 80 and Pluronic® L121 were placed in a glass reactor equipped with an overhead mechanical stirrer and peristaltic pump. In all cases, surfactant ratio was equal to 30 vol% of monomer mixture. The ratio of Span® 80 and Pluronic® L121 in the surfactant mixture were adjusted based on the volume fractions of β-myrcene and 1,4-BDDMA, respectively. Internal phases were prepared by dissolving 1 mol % of KPS (with regards to monomer mole number) and 0.4 g of $CaCl_2.6H_2O$ in 40 mL of ultrapure deionized water. HIPEs were prepared by dispersing internal phase in the continuous phase with the help of a peristaltic pump. During HIPE preparation, pumping rate of the internal phase was set to 50 rpm and emulsification was achieved at a stirring rate of 400 rpm. Once the addition of internal phase completed, stirring was continued for an additional 15 min. Thereafter, HIPEs were transferred into cylindrical glass bottles (h x w = 3 cm x 3 cm) and cured at 60°C for 24 h. In the end, monoliths were removed from the bottles and extracted with ethanol for 24 h. All the samples were dried under vacuum at 40°C until constant weighing was available. Resulting polyHIPEs were named as MBx, where x is designating the formulation number of HIPE. The formulations of thermally-curable HIPEs were given in Table S1 in the Supplementary Information (SI) file.

Photocurable PolyHIPEs

Photocurable HIPEs were prepared by adding 2 wt% (with regards to monomer mixture) of Irgacure 2959 into the continuous phase of HIPEs during emulsion preparation. The composition of monomers and surfactant mixture were similar with the thermally-curable HIPEs. Internal phases, on the other hand were separately prepared by dissolving 0.4 g of $CaCl_2.6H_2O$ in 40 mL of ultrapure deionized water. HIPEs were prepared in an amber glass reactor equipped with an overhead mechanical stirrer and peristaltic pump. During emulsification, pumping rate of the internal phase was set to 50 rpm, while stirring rate was constant at 400 rpm. When the addition of internal phase completed stirring was continued for an additional 15 min. Then photocurable HIPEs were rapidly poured into cylindrical glass containers with dimensions of 0.5 cm x 3 cm (h x w). Photocuring was achieved in a UV-polymerization cabinet (lamp power 300 W, lamb distance: 20 cm) by exposing HIPEs to UV light for 15 min. Resulting polyHIPEs were extracted with ethanol for 24 h and dried under vacuum at 40°C until constant weight was achieved. Photocured polyHIPEs were named as UMBx where x is designating the formulation number of HIPE. The detailed formulations of photocurable HIPEs are given in Table S2 in the Supplementary Information (SI) file.

Characterization

The morphology of polyHIPEs was investigated by ZEISS Supra 40 VP (Zeiss, Germany) model Scanning Electron Microscope (SEM) at different magnification rates. For this aim, polyHIPE samples were first coated with gold to increase electron magnification on the surface of the samples. By using the SEM images, average cavity size (CS) and interconnected pore size (IPS) of each sample were calculated. In order to determine the average cavity size, the diameters of over 100 cavities were measured, whereas interconnected pore size was calculated by taking over 150 measurements. To obtain a more reliable result, each measurement was multiplied with a correction factor ($2/\sqrt{3}$), then the statistical average and error determined [42].

For the determination of Brunauer-Emmett-Teller (BET) specific surface area (δ_{BET}) of the polyHIPEs, Micromeritics Gemini VII Surface Area and Porosity Analyzer (Micromeritics Instrument Corporation, USA) was used. Before the analysis, all the samples were first degassed at 100°C for 24 h, under nitrogen flow on a degassing unit (Micromeritics FlowPrep 060 Sample Degas Unit, Micromeritics Instrument Corporation, USA). BET specific surface area of the polyHIPEs was calculated by applying BET equation on the recorded N_2 adsorption/desorption isotherms. For each polyHIPE sample, BET specific surface area was calculated from the arithmetic average of 3 different measurements conducted by using 3 different specimens.

Thermal stabilities of polyHIPEs were determined via thermogravimetric analysis (TGA) using a Mettler Toledo TGA/DSC 3 + STAR system. For this purpose, TGA analysis was performed between 30°C and 650°C under N_2 flow at a heating rate of 10°C min^{-1}.

For calculating crosslink ratio, density of the monoliths were determined before and after equilibrium swelling experiments according to Archimedes′ principle by using an analytical balance equipped with a density determination kit (Weightlab WSA224T).

Equilibrium Swelling Experiments

For defining the degree of crosslinking of MBx and UMBx monoliths, swelling of the monoliths were studied by following the increase in weight and volume of the monoliths in toluene. For swelling studies, the amount of solvent was adjusted as 1:10 (w/w) for monolith:solvent. Swelling ratio (Q) was calculated according to Eq. 1 as reported by Steindl et al. previously [43]. For this purpose, weight and the dimensions of the swollen monoliths were recorded after 2 h, 4 h, 8 and 24 h. After 24 h, the swollen monoliths were dried at room temperature under vacuum for 72 h and weighed again. Then the mass and the density of the dry monoliths were determined [43–45]. In Eq. 1, V_{sw} is volume of the swollen polymer, V_0 is the volume of dry polymer, Q is the swelling ratio and φ_p (V_{2m}) is polymer volume fraction at swelling equilibrium.

$$Q = \frac{V_{sw}}{V_0} = \frac{1}{\phi_P} \tag{1}$$

Polymer volume fraction in the equilibrium swollen polymer (V_{2m}) was calculated by using Eq. 2 [46, 47]. In this equation, V_p is the ratio of the volume of polymer, V_g is the volume of the swollen polymer or gel at equilibrium, ρ_g is the density of the swollen polymer, ρ_w is the density of toluene, m_g is the mass of the swollen polymer at equilibrium and m_w is the mass of the solvent present in the swollen polymer.

$$v_{2m} = \frac{v_p}{v_g} = \frac{v_g - v_w}{v_g} = 1 - \frac{m_w \rho_g}{\rho_w m_g} \tag{2}$$

V_{2m} values calculated from equilibrium swelling experiments enabled calculation of molecular weight of polymer chains between crosslinks (M_c) with Flory-Rehner Theory given in Eq. 3 [48, 49].

$$M_c = \frac{V_1 \left[(v_{2m})^{1/3} - \left(\frac{2}{f} v_{2m} \right) \right]}{- \left[\ln (1 - v_{2m}) + v_{2m} + \chi_1 (v_{2m})^2 \right]} \tag{3}$$

where χ_1 is the Flory–Huggins's solvent-polymer interaction parameter, V_1 is the molar volume of toluene as a swelling agent and f is the functionality of the crosslinks. $V1$ and f values are 106.4 cm3 mol− 1 and 4, respectively where $\chi 1$ for poly(β-myrcene-co-1,4-BDDMA) was calculated by using Hildebrand Equation given in Eq. 4 [50, 51]:

$$\chi = \frac{V_s}{RT} (\delta_S - \delta_R)^2 \tag{4}$$

In Eq. 4, R is the universal gas constant (1.987 cal K^{-1} mol^{-1}), T is the temperature in Kelvin, V_S is the molar volume of toluene, δ_S is the solubility parameter of toluene, and δ_R is the solubility parameter of poly(β-myrcene-co-1,4-BDDMA). In that frame, δ_R was determined by using the method reported previously [52, 53] and found as 16.28. By adopting the abovementioned values to Eq. 4, χ_1 for poly(β-myrcene-co-1,4-BDDMA) was found as 0.367. Additionally, the functionality of poly(β-myrcene-co-1,4-BDDMA) which referred to active sites of polymer chain for crosslinking is accepted as 4 by referring the active sites of polyisoprene and polyisoprene-based copolymers [54, 55].

Finally, crosslink density of the monoliths (ν) was calculated by using Eq. 5 [48, 53–56].

$$M_c = \frac{\rho_p}{\nu} \tag{5}$$

Results and Discussion

The presence of three reactive double bonds in β-myrcene make this bio-sourced compound suitable for polymerization through FRP mechanism by thermal-initiation or UV-vis radiation. On the other hand, the use of acrylates in HIPE formulation reduce polymerization shrinkage and leads formation of a more elastic material. Herein, to prepare a polyHIPE by using a terpene, β-myrcene was copolymerized with 1,4-BDDMA within the continuous phase of HIPEs. Polymerization of HIPEs were performed either by thermal-initiation or photoinitiation. Accordingly, thermally-initiated copolymerization of β-myrcene with 1,4-BDDMA was first performed by varying the ratio of β-Myrcene:1,4-BDDMA from 10:90 to 90:10 in the presence of a water-soluble thermal initiator (KPS). In the end, for all monomer ratios, stable HIPE templates were prepared and solid monoliths with porous structure were obtained after polymerization. Since the particular focus of the work is obtaining sustainable polyHIPEs through photopolymerization, the similar HIPE formulations was also used to prepare photocurable terpene-containing HIPE formulations. The only difference in the formulations was using a photoinitiator (Irgacure 2959), instead of thermal-initiator (KPS). Afterall, stable HIPEs were obtained in all cases. However, photocurable HIPE template having 10:90 ratio of β-Myrcene:1,4-BDDMA did not yield a solid polyHIPE monolith. For the β-Myrcene:1,4-BDDMA ratios changing between 20:80 to 90:10, open porous polyHIPEs were obtained by photocuring of HIPEs.

To evaluate the effect of polymerization procedure on the pore morphology, SEM images of thermally cured

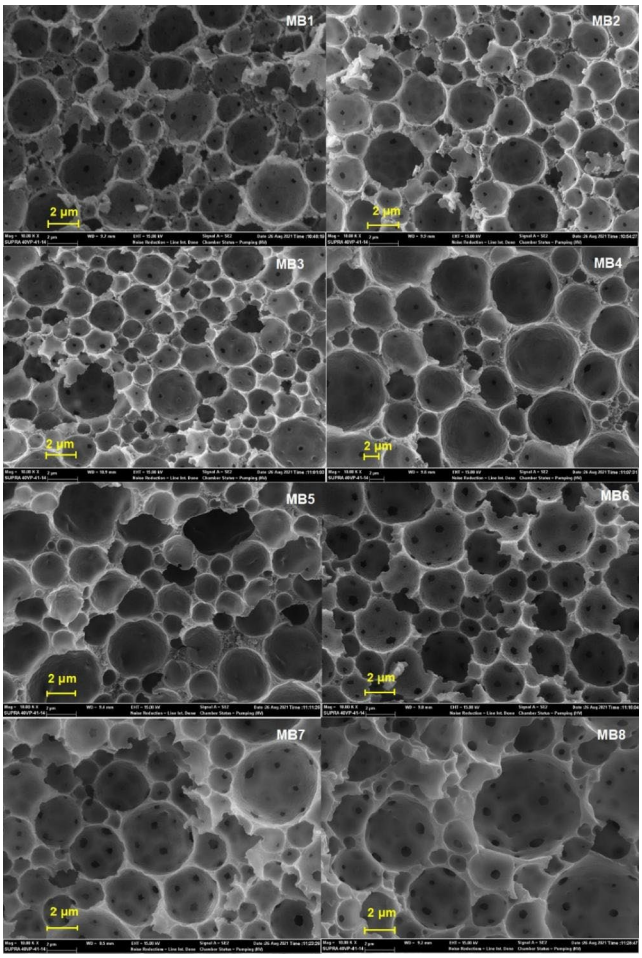

Fig. 1 SEM images of MBx monoliths obtained from HIPEs having *β*-myrcene at varying ratios from 10 to 80 at a magnification rate of 10.00 K X (EHT = 15.00 kV, Signal A = SE2).

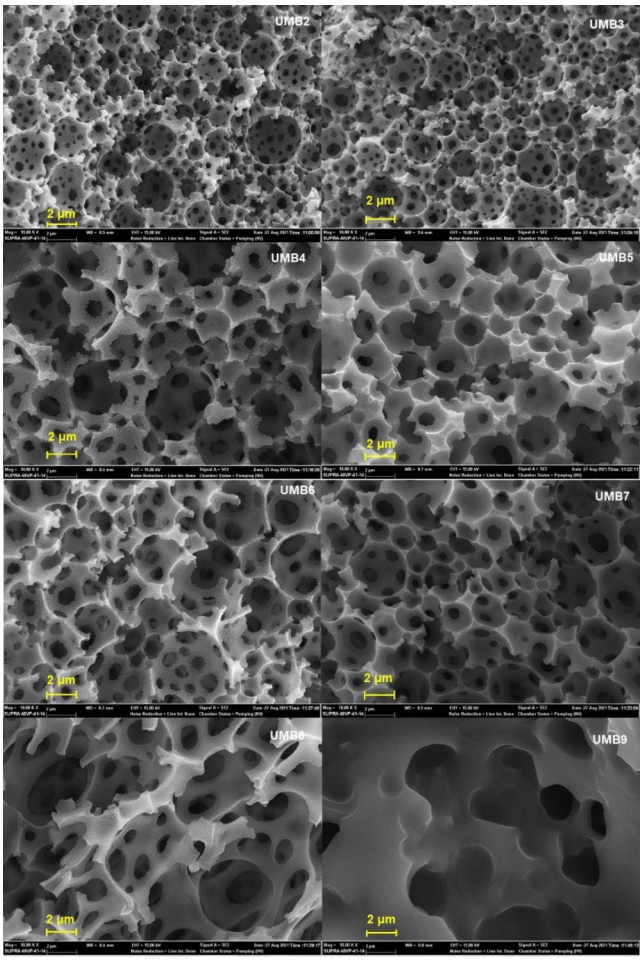

Fig. 2 SEM images of UMBx monoliths obtained from HIPEs having *β*-myrcene at varying ratios from 20 to 90 at a magnification rate of 10.00 K X (EHT = 15.00 kV, Signal A = SE2).

polyHIPEs (MBx monoliths) and photocured polyHIPEs (UMBx monoliths) are given in Figs. 1 and 2, respectively. Additionally, cavity size and interconnected pore size of the thermally cured and photocured polyHIPEs which were calculated from SEM images are given in Table 1, comparatively. When the obtained monoliths are compared in terms of cavity size, thermally cured polyHIPEs were found to exhibit more homogenous and uniform pore structure than photocured polyHIPEs. On the other hand, the SEM images presented in Fig. 2 clearly show that there is a much greater number of interconnecting pores between the cavities in photocured polyHIPEs. According to Table 1, in photocured polyHIPEs when the amount of *β*-myrcene was increased from 20 vol% to 90 vol%, average cavity size and interconnected pore size was increased from 3.21 to 12.22 µm, and from 0.76 to 2.57 µm, respectively. This result can be supported by the comparison of the SEM images of UMB2 and UMB9 monoliths. Herein, variation of pore morphology can be explained based on different phenomena including locus of initiation, monomer polarity and polymerization kinetics.

The locus of initiation is the driving force affecting morphology and molecular structure of polyHIPEs [57]. As it is well-known from previous studies, the use of water-soluble initiators provides interface-initiated polymerization which tends to form closed-cell polyHIPEs [2]. It can be seen from the SEM images presented in Fig. 1 that the pore morphology of thermally cured polyHIPEs is also variated from closed to more open due to the increasing number of interconnected pores. On one hand, this variation can be attributed to increase in the amount of *β*-myrcene in the monomer composition. On the other hand, this result might be also explained by the difference between the monomer polarities. Since *β*-myrcene is a hydrophobic monomer, it tends to present in the oil phase. But, 1,4-BDDMA has relatively higher polarity and it tends to diffuse to aqueous phase. When a water-soluble thermal initiator is used, primary monomer radicals are formed in the aqueous phase

Table 1 Cavity size (CS), interconnected pore size (IPS) and BET specific surface area (δ_{BET}) of MBx and UMBx monoliths

PHP	β-myrcene (vol%)	1,4-BDDMA (vol%)	δ_{BET} (m^2g^{-1})	CS (μm)	IPS (μm)
MB1	10	90	24.03	5.44 ± 0.18	0.35 ± 0.01
MB2	20	80	26.07	3.88 ± 0.11	0.41 ± 0.01
MB3	30	70	24.60	4.03 ± 0.06	0.41 ± 0.01
MB4	40	60	17.19	5.88 ± 0.13	0.39 ± 0.01
MB5	50	50	13.57	5.94 ± 0.13	-
MB6	60	40	16.20	5.18 ± 0.10	0.79 ± 0.01
MB7	70	30	6.03	5.35 ± 0.14	0.83 ± 0.02
MB8	80	20	4.01	5.60 ± 0.16	0.92 ± 0.02
MB9	90	10	0.53	-	5.44 ± 0.19
UMB1	10	90	-	-	-
UMB2	20	80	12.89	3.21 ± 0.10	0.76 ± 0.02
UMB3	30	70	13.34	2.62 ± 0.06	0.77 ± 0.02
UMB4	40	60	4.50	5.35 ± 0.12	1.69 ± 0.03
UMB5	50	50	4.51	4.72 ± 0.11	1.16 ± 0.03
UMB6	60	40	4.33	5.67 ± 0.13	1.46 ± 0.03
UMB7	70	30	2.86	5.55 ± 0.12	0.93 ± 0.03
UMB8	80	20	1.63	8.27 ± 0.19	2.29 ± 0.12
UMB9	90	10	0.29	12.22 ± 0.41	2.57 ± 0.10

by the attack of initiator radicals to the 1,4-BDDMA monomers diffused to this phase. This primary monomer radicals are diffused to the oil-water interface and initiated the free radical copolymerization crosslinking (FRCPXL) reaction between β-myrcene and 1,4-BDDMA. When the ratio of hydrophobic monomer increased, oil phase become the source of monomer units for the growing polymer chains and propagation reactions inclined to proceeded at the oil phase. Therefore, more open porous structure is formed with the increase of β-myrcene in the monomer composition. Here, we also believe that primary monomer radicals containing 1,4-BDDMA units play a major role in the initiation and propagation steps of polymerization. In our experience, FRCPXL of HIPEs containing β-myrcene is only possible in the presence of comonomers containing flexible units. Flexible comonomer units prevent steric hindrance and crosslinked polymer networks are formed. Otherwise, the gel point cannot be reached, and solidification does not occur [41].

In a typical polyHIPE with a hierarchical porous structure, the first level of pores (cavities) is reflecting emulsion droplets. During polymerization, a continuous polymer film is formed around the emulsion droplets. Removal of the dispersed phase leads the formation of cavities. Accordingly, cavity size distribution is a clue for emulsion stability. Polymerizing of emulsions that could maintain stability until the gel point leads smaller cavities, and homogeneous cavity size distribution. Secondary pores (interconnections, pore throats or holes) are formed by the rupture of the polymer film from the closest and thinnest point between the

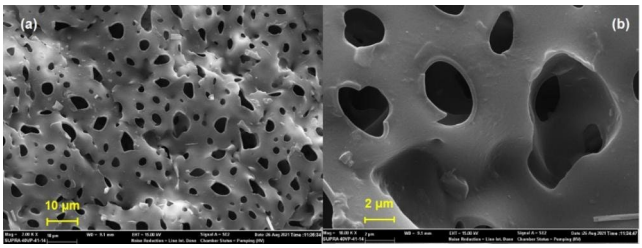

Fig. 3 SEM images of MB9 monolith at a magnification rate of (a) 2.00 K X ; (b) 10.00 K X (EHT = 15.00 kV, Signal A = SE2).

adjacent droplets. Formation of interconnected pores was also explained based on volume contraction during the conversion of vinylic monomer units to polymer chains [5, 58, 59]. On the other hand, Menner and Bismarck suggested that incompressible droplet phase prevent shrinking during polymerization of HIPE and holes are formed by a mechanical process due to the rupture of polymer film surrounding the droplets [60]. Herein, due to rapid initiation and high monomer-polymer conversion rate, photocurable UMBx monoliths are exhibiting more uniform open-cellular morphology [61]. However, the change of average cavity size and interconnected pore size in UMBx monoliths are found to be more susceptible to monomer composition as compared to MBx monoliths. As a result, the average cavity size of MBx monoliths were changed slightly with the increasing β-myrcene amount, while a more significant change was observed for UMBx monoliths. Additionally, in both cases, high β-myrcene ratio caused widening of cavities. In this respect, different than others, the morphology of thermally cured MB9 monolith constitutes from small holes, where the borders of the cavities cannot be identified (Fig. 3). This situation suggest that emulsion stability is broken until the gel point reached during polymerization. Maintaining emulsion stability is an important parameter for locking the emulsion geometry before polymerization. Long curing times create an opportunity for change in internal geometry before the gel point is reached. At high ratios, β-myrcene tend to add its own monomer to the growing copolymer chains due to high monomer reactivity, which leads delayed gel effect [41]. In addition, the cavity walls may collapse during drying due to the shrinkage of polymyrcene chains with elastomer property [62, 63]. Similarly, the larger cavities observed in UMB8 and UMB9 can be also explained due to emulsion stability. Consistent with these findings, BET specific surface area (δ_{BET}) of MBx and UMBx monoliths presented in Table 1 also found to be decreased as the amount of β-myrcene increased.

Crosslink density is a parameter playing an important role in featuring final characteristic properties of materials such as morphology and swelling [64]. In order to investigate the crosslink density of a polymer network, equilibrium swelling experiments should be performed in an

Table 2 Swelling ratio (Q), foam density (ρ), polymer volume fraction in the swollen mass (V_{2m}), molecular weight between crosslinks (M_c), and crosslink density (υ) for MBx monoliths

PHP	Q	ρ (g cm^{-3})	V_{2m}	M_c (g mol^{-1})	υ (mol cm^{-3})
MB1	2.69	0.27	0.24	4026.94	7.01×10^{-4}
MB2	3.33	0.28	0.19	6310.88	6.06×10^{-4}
MB3	3.52	0.31	0.20	6367.67	7.57×10^{-4}
MB4	3.80	0.24	0.19	7077.55	8.23×10^{-4}
MB5	3.57	0.24	0.20	6446.88	1.06×10^{-3}
MB6	3.94	0.30	0.17	8353.12	9.36×10^{-4}
MB7	3.04	0.27	0.21	5350.14	1.65×10^{-3}
MB8	1.27	0.39	0.39	1167.20	8.41×10^{-3}
MB9	1.52	0.83	0.37	1315.72	8.22×10^{-3}

Table 3 Swelling ratio (Q), foam density (ρ), polymer volume fraction in the swollen mass (V_{2m}), molecular weight between crosslinks (M_c), and crosslink density (υ) for UMBx monoliths

PHP	Q	ρ (g cm^{-3})	V_{2m}	M_c (g mol^{-1})	υ (mol cm^{-3})
UMB2	3.51	0.65	0.19	6732.48	9.68×10^{-5}
UMB3	4.47	0.70	0.14	11625.40	6.06×10^{-5}
UMB4	5.64	0.52	0.11	20818.33	2.52×10^{-5}
UMB5	5.30	0.56	0.15	12177.33	4.61×10^{-5}
UMB6	6.58	0.47	0.09	33284.59	1.43×10^{-5}
UMB7	3.15	0.56	0.21	5367.52	1.06×10^{-4}
UMB8	2.55	0.54	0.24	4173.41	1.31×10^{-4}
UMB9	2.07	0.82	0.26	3325.37	2.47×10^{-4}

appropriate solvent. In this respect, swelling ratio (Q) of MBx and UMBx monoliths were determined using toluene as a swelling agent to investigate the crosslink density. During equilibrium swelling experiments, alterations on the mass of the monoliths within 2 h, 4 h, 8 h and 24 h were recorded. The images of MBx and UMBx monoliths before swelling and after swelling for 24 h are given as a supplementary file (Figure S1, S2, S3 and S4). The calculated swelling ratio of MBx and UMBx monoliths are tabulated in Tables 2 and 3, respectively. Depending on Tables 2 and 3, it can be concluded that as the ratio of *β*-myrcene increased, swelling ratio of the monoliths decreased. Especially, for the MBx and UMBx monoliths obtained from HIPEs having *β*-myrcene ratio between 30 and 60%, swelling ratio was found to reach the highest value. On the other hand, MB8 and MB9 monoliths obtained from HIPEs having 80 and 90% *β*-myrcene had shown the lowest swelling ratio. As it is well-known, the degree of swelling for a polymer network is usually changed inversely with the degree of crosslinking. If a highly crosslinked polymer network is involved, swelling degree is decreased. By adopting the swelling data in Flory-Rehner theory, the physicochemical parameters of a polymer network such as polymer volume fraction in the swollen mass (V_{2m}), molecular weight between crosslinks (M_c) and crosslink density (υ) of MBx and UMBx monoliths can be calculated to estimate the degree of crosslinking in the polymer network. However, due to the approximated assumptions have been made in Flory-Rehner theory, this calculation is prone to errors. Therefore, the data obtained is not certain and can be only used to get qualitative information [43]. In this context, to make an estimation of the variation of crosslink density depending on the monomer composition, the polymer volume fraction in the swollen mass (V_{2m}), molecular weight between crosslinks (Mc) and crosslink density (υ) of MBx and UMBx monoliths were calculated approximately using Flory-Rehner theory. Accordingly, the obtained data and the foam densities determined via Archimedes′ principle for MBx and UMBx monoliths are respectively tabulated in Tables 2 and 3.

Depending on the variation of polymer volume fraction in the swollen mass (V_{2m}) of MBx and UMBx monoliths, monomer-polymer conversion of the polyHIPEs determined to be increased by the increment in the ratio of *β*-myrcene. It can be seen by the comparison of V_{2m} values presented in Tables 2 and 3 that monoliths prepared by the polymerization of HIPEs with highest *β*-myrcene concentration, namely MB9 and UMB9, have higher V_{2m}. Furthermore, Tables 2 and 3 also shows that the crosslink density (υ) increased while molecular weight between crosslinks (Mc) decreased in both thermally cured and photocured monoliths. The reason of this alteration can be explained by the formation of a more entangled polymer network with more crosslink points. Especially, crosslink density of UMBx monoliths were found to be lower than MBx monoliths due to rapid initiation of photopolymerization [65, 66].

In a highly crosslinked polymer network, by an increment in crosslink density, polymer chain movements are restricted, and solvent could not interact with polymer chains, hence resulted with a decrease in swelling capacity [45, 67]. The reason of low swelling ratio and high crosslink density of MB9 and UMB9 monoliths could be explained depending on that issue. On the other hand, this alteration on crosslink density could not be only accepted as a sign of copolymerization of *β*-myrcene and 1,4-BDDMA. In addition to this, when the ratio of *β*-myrcene in the monomer composition is significantly higher than 1,4-BDDMA, it tends to add its own kind to the growing chains, due to the higher monomer reactivity. These reactions result with the formation of polymyrcene chains having different microstructures beside poly(*β*-myrcene-co-1,4-BDDMA) chains [28, 68]. However, by the formation of polymyrcene chains, which has a similar structure with isoprene, leads shrinkage of polymer network. Resultingly, while the pores and cavities are collapsed, swelling degree of the polymer network is also decreased [29, 30, 69].

The density of the polymer foams is given in Tables 2 and 3. As can be seen from related tables, the density of the

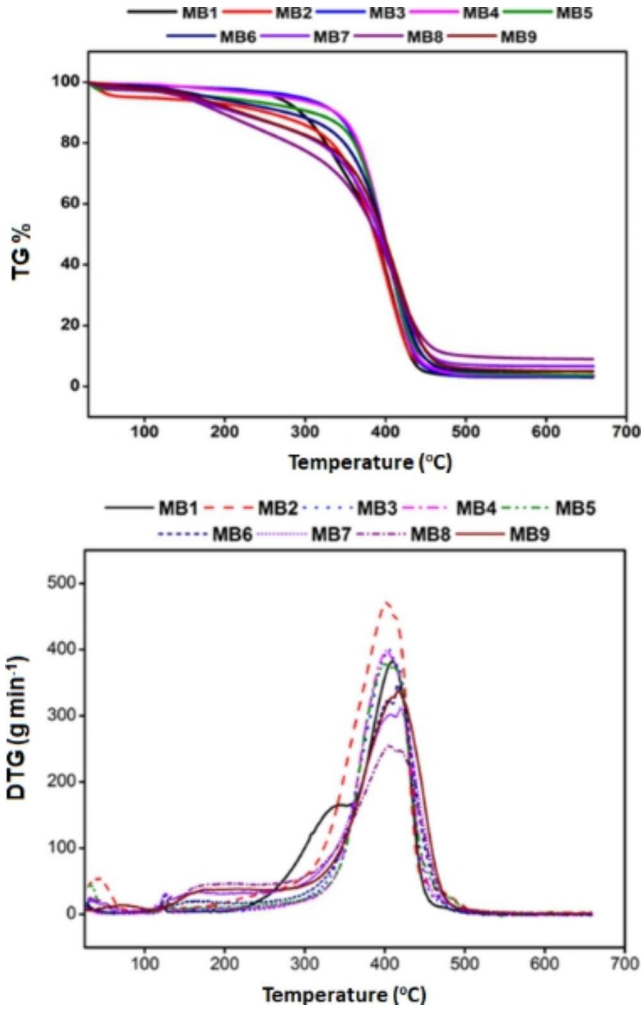

Fig. 4 TG and DTG curves of MBx monoliths

polymer monoliths increased as the amount of *β*-myrcene in the monomer composition increased. Moreover, density of resulting polyHIPEs is determined to be higher than expected. Indeed, polyHIPEs usually exhibit densities lower than 0.1 g cm^{-3} [5]; additionally depending on Eq. 5, density of the polymers is expected to decrease by the increase of crosslink density. Herein, density of the resulting polyHIPEs is increased with the increase in crosslinking density. The reason of this unusual change can be explained due to the formation of polymyrcene moieties with different microstructures at high *β*-myrcene ratios. Moreover, at high degree of crosslinking, average distance between two crosslink points decreases, which also lead a decrease in polymer free volume [63, 70, 71].

Indeed, the presence of polymyrcene and poly(*β*-myrcene-co-1,4-BDDMA) also proved by thermal degradation analysis of MBx and UMBx monoliths. TG and DTG curves of MBx and UMBx monoliths are given in Figs. 4 and 5, respectively. According to the thermograms presented in Fig. 4, the thermal degradation of MBx monoliths can

Table 5 Maximum thermal degradation temperature (T_{max}) of MBx and UMBx monoliths

PHP	T_{max} (°C)	PHP	T_{max} (°C)
MB1	411.9	UMB1	-
MB2	415.5	UMB2	413.3
MB3	414.7	UMB3	416.9
MB4	415.5	UMB4	417.7
MB5	416.7	UMB5	418.7
MB6	420.9	UMB6	415.4
MB7	424.5	UMB7	416.6
MB8	421.4	UMB8	415.3
MB9	420.9	UMB9	415.6

be evaluated in three different temperature zones: 0-100°C, 100-250°C, 250-500°C. The mass loss detected under 100°C generally indicated the presence of volatile products, water, or a solvent. However, the second degradation step observed between 100-250°C can be accepted as a clue for the formation of polymyrcene homopolymer, due to the tendency of *β*-myrcene monomer adding its own kind to the growing chains [72, 73]. This degradation step was observed in monoliths prepared from HIPEs containing *β*-myrcene higher than 60% in the monomer composition such as MB7, MB8 and MB9. According to DTG thermograms given in Fig. 4 and the data presented in Table 5, the maximum degradation rate has been reached between ~411°C and 421°C for MBx monoliths. Table 5 shows that the maximum degradation temperature (T_{max}) of MBx monoliths is slightly different from each other, most probably due to the formation of different polymer microstructures at different monomer compositions. Additionally, as the amount of *β*-myrcene in the monomer composition increases, the maximum degradation temperature shifts to higher temperatures and the rate of degradation decreases. On the other hand, as different than the others, MB1 monolith exhibits an additional degradation step between 250°C and 360°C. This additional step might be attributed to the degradation of poly(1,4-butanediol dimethacrylate) (PBDDMA) homopolymer.

Thermograms presented in Fig. 5 indicates that UMBx monoliths are subjected to two-step degradation. The DTG thermograms of UMBx monoliths presented in Fig. 5 and the data given in Table 5 reveals that the maximum degradation rate has been reached between 413-419°C. However, as similar with the MBx monoliths, the amount of degraded polymer at the maximum degradation temperature in UMBx monoliths obtained from HIPEs with a *β*-myrcene ratio more than 70% is lower due to the presence of polymyrcene homopolymer. Depending on the reaction temperature and regioselectivity, three different microstructures of polymyrcene (1,2 – 1,4- and 3,4-polymyrcene) may occur [62, 74]. Accordingly, as the amount of *β*-myrcene in the monomer composition increases, the rate of degradation decreases. In addition, when the maximum degradation temperatures

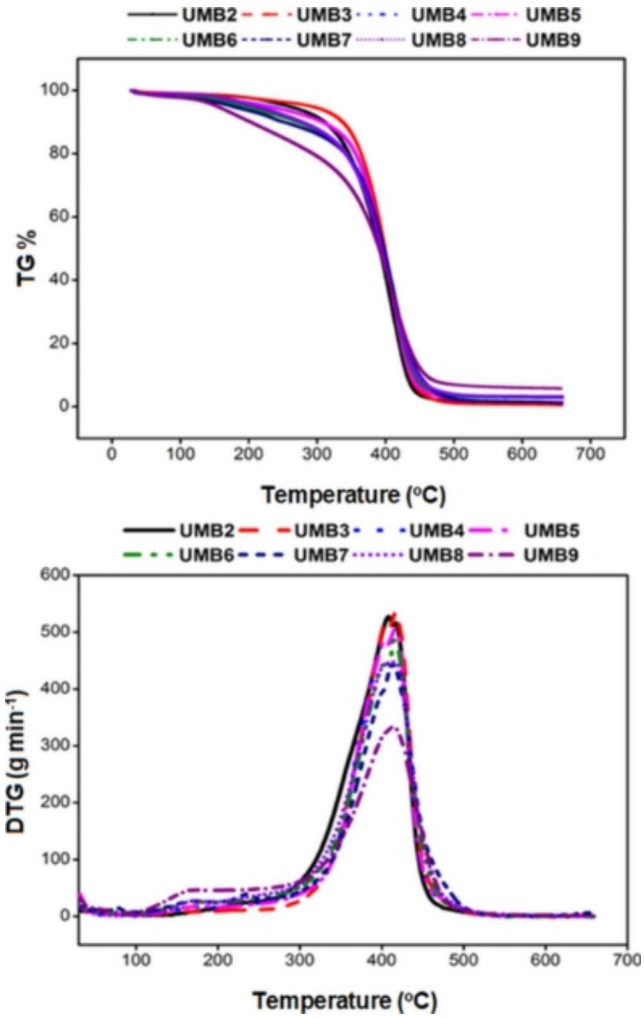

Fig. 5 TG and DTG curves of UMBx monoliths

(T_{max}) of MBx and UMBx monoliths (Table 5) are compared, it can be concluded that MBx monoliths with higher crosslink density undergo thermal degradation at slightly higher temperatures.

Conclusion

In the present study, the influence of curing method and monomer composition on the pore morphology and crosslink density of polyHIPEs, obtained from β-myrcene and 1,4-BDDMA containing-HIPEs has been demonstrated. It has been revealed that the morphological features are greatly dependent on the monomer composition and curing approach. It has been observed once again that the high monomer reactivity and regioselectivity of β-myrcene poses a major challenge for the formation of highly crosslinked polyHIPE network by free radical copolymerization. However, photocuring has led hierarchical open porous morphology due to rapid polymerization rate. Accordingly, it has been shown that photocuring is a convenient and an efficient way for the synthesis sustainable polyHIPEs using β-myrcene. Future work will focus on the synthesis of sustainable polyHIPEs through photopolymerization of HIPEs prepared entirely from terpene-based monomers.

Supplementary Information The online version contains supplementary material available at https://doi.org/10.1007/s10924-023-02855-5.

Author Contribution B.K. and E.H.M. conceived and planned the experiments. M.S. carried out experimental study. B.K. wrote the manuscript with the support of E.H.M. B.K. supervised the project under the consultancy of E.H.M. The critical feedback, discussion of analysis and manuscript the experimental studies of this work was provided by E.H.M. and B.K.

Funding This study is supported financially by The Scientific and Technological Research Council of Turkey (TÜBİTAK) through the project number 120Z433.

Declarations

Competing interests The authors declare that there has been no competing financial interests or personal relationships that could have appeared to influence this study.

References

1. Barby D, Haq Z (1982) Low density porous cross-linked polymeric materials and their preparation,European Patent(Unilever).
2. Zhang T, Sanguramath RA, Silverstein MS (2019) Macromolecules 52:5445–5479. https://doi.org/10.1021/acsami.9b10467
3. Gui H, Zhang T, Guo Q, (2019) ACS Appl Mater Interfaces 11:39, 36063–36072. https://doi.org/10.1021/acsami.9b10467
4. Zhang T, Zhao Y, Silverstein MS (2020) Cellulose 27:4007–4018. https://doi.org/10.1007/s10570-020-03059-z
5. Cameron NR (2005) Polymer 46:1439–1449. https://doi.org/10.1016/j.polymer.2004.11.097
6. Mert EH, Mert HH (2020) Polym Comp 42:724–738. https://doi.org/10.1002/pc.25861
7. Mahadik DB, Lee KY, Ghorpade RV (2018) Sci Rep 8:16783. https://doi.org/10.1038/s41598-018-34997-1
8. Muchan P, Saiwan C, Demontigny D, Tontiwachwuthikul P (2013) Chem Eng Trans 35:391–396. https://doi.org/10.3303/CET1335065
9. Jerenec S, Šimić M, Savnik A, Podgornik A, Kolar M, Turnšek M, Krajnc P (2014) React Func Polym 78:32–37. https://doi.org/10.1016/j.reactfunctpolym.2014.02.011
10. Choudhury S, Fitzhenry L, White B, Connolly D (2016) Materials 9(3):212. https://doi.org/10.3390/ma9030212
11. Ashvini B, Deshmukh A, Nalawade C, Karbhal I, Qureshi MS, Shelke MV (2018) Carbon 128:287–295. https://doi.org/10.1016/j.carbon.2017.11.080
12. Mert HH (2020) Int J Energy Res 44:6583–6594. https://doi.org/10.1002/er.5390
13. Kramer S, Cameron NR, Krajnc P (2021) Polymers 13:1786. https://doi.org/10.3390/polym13111786

14. Ferrández-Montero A, Carlier B, Agniel R, Leroy-Dudal J, Vancaeyzeele C, Plesse C (2021) J Mater Chem C 9:36, 12388–12398. https://doi.org/10.1039/D1TC01846A
15. Barbetta A, Dentini M, Zannoni EM, De Stefano ME (2005) Langmuir 21, 12333–12341 https://doi.org/10.1021/la303788z
16. Silverstein MS (2014) Polymer 55:304–320. https://doi.org/10.1016/j.polymer.2013.08.068
17. Silverstein MS (2017) Polymer 126:261–282. https://doi.org/10.1016/j.polymer.2017.07.046
18. Israel S, Levin M, Oliel S, Mayer D, Lerner I, Silverstein MS (2022) Macromolecules 55(6):1992–2002. https://doi.org/10.1021/acs.macromol.1c01432
19. Huš S, Kolar M, Krajnc P (2015) Des Monomers Polym 18:698–703. https://doi.org/10.1080/15685551.2015.1070503
20. Shengmiao Z, Jianding C, Victoria PT (2008) Lett Org Chem 5(4):304–307. https://doi.org/10.2174/157017808784049443
21. Lovelady E, Kimmins SD, Wub J, Cameron NR (2011) Polym Chem 2:559. https://doi.org/10.1039/C0PY00374C
22. Hobiger V, Paljevac M, Krajnc P (2022) Polymer 14:7. https://doi.org/10.3390/polym14071338
23. Langford CR, Johnson DW, Cameron NR (2014) Polym Chem 5:21, 6200–6206. https://doi.org/10.1039/C4PY00713A
24. Chen C, Eissa AM, Schiller TL, Cameron NR (2017) Polymer 126:395–401. https://doi.org/10.1016/j.polymer.2017.04.021
25. Lebedevaite M, Talacka V (2021) J Ostrauskaite J Appl Polym Sci 138:16. https://doi.org/10.1002/app.50233
26. Thomsett MR, Storr TE, Monaghan OR, Stockman RA, Howdle SM (2016) Green Mat 4:115–134. https://doi.org/10.1680/jgrma.16.00009
27. Della Monica F, Kleij AW (2020) Polym Chem 11:5109–5127. https://doi.org/10.1039/D0PY00817F
28. Trumbo DL (1993) Polym Bull 31:629–636
29. Sarkar P, Bhowmick AK (2019) J Polym Sci Part A: Polymer Chemistry 57:738–751. https://doi.org/10.1002/pola.29320
30. Sahu P, Bhowmick AK, Kali G (2020) Processes 8:553. https://doi.org/10.3390/pr8050553
31. Sahu P, Sarkar P, Bhowmick AK, (2018) ACS Sust Chem Eng 6(5):6599–6611. https://doi.org/10.1021/acssuschemeng.8b00383
32. Wilbon P, Chu F, Tang C (2013) Macromol Rapid Comm 34(1):8–37. https://doi.org/10.1002/marc.201200513
33. Weems AC, Delle Chiaie KR, Yee R, Dove AP (2020) Biomacromolecules 21:163–170. https://doi.org/10.1021/acs.biomac.9b01125
34. Matic A, Schlaad H (2018) Polym Int 67:500–505. https://doi.org/10.1002/pi.5534
35. Firdaus M, Montero de Espinosa L, Meier MAR (2011) Macromolecules 44:7253–7262. https://doi.org/10.1021/ma201544e
36. Tarablesi B, Jasinski F, Lobry E, Chemtob A, Nouen D, Criqui A (2015) Green Mater 3:1–26. https://doi.org/10.1680/gmat.15.00015
37. Claudino M, Mathevet JM, Jonsson M, Johansson M (2013) Bringing D-Limonene to the scene of Bio-Based Thermoset Coatings via Free-Radical Thiol–Ene Chemistry: Macromonomer Synthesis, UV-Curing and Thermo–Mechanical characterization. Polymer Chemistry (RSC Publishing)
38. Carrodeguas LP, Martín C, Kleij AW (2017) Macromolecules 50:5337–5345. https://doi.org/10.1021/acs.macromol.7b00862
39. Bauer N, Brunke J, Kali G, Sust ACS (2017) Chem Eng 5:11. https://doi.org/10.1021/acssuschemeng.7b02091
40. Metafiot A, Kanawati Y, Ge JF, rard B, Defoort M, Maric (2017) Macromolecules, 50:8, 3101 – 3120 https://doi.org/10.1021/acs.macromol.6b02675
41. Mert EH, Kekevi B (2020) Colloid Polym Sci 298:1423–1432. https://doi.org/10.1007/s00396-020-04730-4
42. Barbetta A, Cameron NR (2004) Macromolecules 37:3188–3201. https://doi.org/10.1021/ma0359436
43. Steindl P, Menner A, Bismarck A (2022) Polymer 240:124476. https://doi.org/10.1016/j.polymer.2021.124476
44. Schreiber HP, Holden HW, Barna G (1970) J Polym Sci Part C 30:471–484. https://doi.org/10.1002/polc.5070300151
45. Witono JR, Noordergraaf I, Heeres HJ, Janssen LPBM, Heeres H (2014) Carbohydr Polym 103:325–332. https://doi.org/10.1016/j.carbpol.2013.12.056
46. Neuburger NA, Eichinger BE (1988) Macromolecules 21:3060–3070. https://doi.org/10.1021/ma00188a026
47. Peppas NA, Huang Y, Torres-Lugo M, Ward JH, Zhang J (2000) Annu Rev Biomed Eng 2:9–29. https://doi.org/10.1146/annurev.bioeng.2.1.9
48. Flory PJ (1953) Principles of polymer chemistry. Cornell University Press, Ithaca, NY
49. Van Krevelen DW, Te K, Nijenhuis (2009) Properties of polymers: their correlation with chemical structure; their numerical estimation and prediction from additive group contributions. Elsevier, Netherlands
50. Hildebrand JH, Scott RL (1950) The solubility of Nonelectrolytes. Rheinhold Publishing Corporation, New York
51. Sarkar P, Bhowmick AK, (2016) ACS Sust Chem Eng 4:5462–5474. https://doi.org/10.1021/acssuschemeng.6b01038
52. Hansen CM (1967) J Paint Technol 39:104–117
53. Gharagheizi F, Eslamimanesh A, Mohammadi AH, Richon D (2011) Ind Eng Chem Res 50:10344–11034
54. Hiranobe CT, Ribeiro GD, Torres GB, Prado dos Reis EA, Cabrera FC, Job AE, Paima LL, dos Santos RJ (2021) Mater Res 24:1, e20210041. https://doi.org/10.1590/1980-5373-MR-2021-0041.
55. Kim DY, Park JW, Lee DY, Seo KH (2020) Polym 12(9):2020. https://doi.org/10.3390/polym12092020
56. Flory PJ, Rehner J (1943) J Chem Phys 11:512. https://doi.org/10.1063/1.1723791
57. T.Gitli MS (2008) Soft Matter 4:2475–2485. https://doi.org/10.1039/B809346F
58. Cameron NR, Sherrington DC, Albiston L, Gregory DP (1996) Colloid Polym Sci 274:592–595. https://doi.org/10.1007/BF00655236
59. Hainey P, Huxham IM, Rowatt B, Sherrington DC, Tetley L (1991) Macromolecules 24:117–121. https://doi.org/10.1021/ma00001a019
60. Menner A, Bismarck A (2006) Macromol. Symp. 242, 19–24 https://doi.org/10.1002/masy.200651004
61. Kim S, Kim JQ, Choi SQ, Kim K (2022) Polym Chem 13:492–500. https://doi.org/10.1039/D1PY01175H
62. Sarkar P, Bhowmick AK (2014) RSC Adv. 4, 61343 – 61354 https://doi.org/10.1039/C4RA09475A
63. Sarkar P, Bhowmick AK, Sust ACS (2016) Chem Eng 4:2129–2141. https://doi.org/10.1021/acssuschemeng.5b01591
64. Hernandez-Ortiz JC, Vivaldo-lima E (2013) Cross-linking. In: Saldivar-Guerra E, Vivaldo-Lima E (eds) Handbook of polymer synthesis, characterization and processing, 1st edn. John Wiley & Sons, Inc., Hoboken, NJ, USA, pp 187–204
65. Harikrishnaa R, Shaikha AW, Ponrathnama S, Rajana CR, Bhongale S (2014) Des Monomers Polym 17(1):1–6. https://doi.org/10.1080/15685551.2013.771312
66. Elbadawy AK, Alaa E, Menzeld H, Chen X (2018) Int J Bio Macromolecules 120:1884–1892. https://doi.org/10.1016/j.ijbiomac.2018.10.011
67. Afinjuomo F, Barclay TG, Song Y, Parikh A, Petrovsky N, Garg S (2019) React Func Polym 134:104–111. https://doi.org/10.1016/j.reactfunctpolym.2018.10.014
68. Hulnik MI, Vasilenko IV, Radchenko AV, Peruch F, Ganachaud F, Kostjuk SV (2018) Polym Chem 9:48, 5690–5700. https://doi.org/10.1039/C8PY01378K

69. Robles-Dutenhefner PA, Speziali MG, Sousa EMB, dos Santos EN, Gusevskaya EV (2005) Appl Cat A: General 295:52–58. https://doi.org/10.1016/j.apcata.2005.08.005
70. Tarablsi B, Jasinski F, Lobry E, Chemtob A, Le Nouen D, Criqui A (2015) Green Mat 3(3):93–101. https://doi.org/10.1680/jgrma.15.00015
71. Hoti G, Caldera F, Cecone C, Pedrazzo AR, Anceschi A, Appleton SL, Khazaei Monfared Y, Trotta F (2021) Materials 14:478. https://doi.org/10.3390/ma14030478
72. Johanson AJ, Mckennon FL, Goldblatt A (1948) Ind Eng Chem 40(3):500–502. https://doi.org/10.1021/ie50459a033
73. Marvel CS, Hwa CCL (1960) J Polym Sci 45:25–34. https://doi.org/10.1002/pol.1960.1204514503
74. Metafiot A, Gerard JF, Defoort B, Maric M (2018) J Polym Sci Part A: Polym Chem 56:8. https://doi.org/10.1002/pola.28963